Topics in Catalysis
https://doi.org/10.1007/s11244-021-01537-7

ORIGINAL PAPER

Polyaniline-Manganese Ferrite Supported Platinum–Ruthenium Nanohybrid Electrocatalyst: Synergizing Tailoring Toward Boosted Ethanol Oxidation Reaction

Fatemeh Karimi[1] · Mohsen Ghorbani[2] · Mohammad Soleimani Lashkenari[3] · Masoomeh Jajroodi[4] · Elahe Fallah Talooki[2] · Yasser Vaseghian[1] · Onur Karaman[5] · Ceren Karaman[6]

Accepted: 9 November 2021
© The Author(s), under exclusive licence to Springer Science+Business Media, LLC, part of Springer Nature 2021

Abstract

Tailoring effective electrocatalysts for the ethanol oxidation process with low-price, high electrocatalytic activity, and long lifetime is crucial for large-scale application of direct ethanol fuel cells. Herein, it was aimed to provide a facile method for designing Polyaniline-Manganese ferrite (PANI-$MnFe_2O_4$) supported nanocatalysts modified with Pt/Ru to be utilized for ethanol electrooxidation. The successful synthesis of the PANI-$MnFe_2O_4$/Pt/Ru nanocomposite was confirmed by the physicochemical analysis techniques including Fourier transform infrared spectroscopy, field emission scanning electron microscopy, and X-ray diffraction. The electrooxidation of ethanol at room temperature was investigated using a number of electrochemical characterizations such as cyclic voltammetry, linear sweep voltammetry, and chronoamperometry techniques. In comparison to other electrodes, the PANI-$MnFe_2O_4$/Pt–Ru electrode demonstrated superior efficiency in terms of boosting forward current (I_f, 100 $mAcm^{-2}$) and increasing the electrochemically active surface area (ECSA, 30.3) that was required for ethanol molecules during the oxidation process. Furthermore, results demonstrated that introducing Ru and Pt to the PANI-$MnFe_2O_4$ support enhanced its efficiency towards the ethanol oxidation reaction by boosting both the stability (94%) and the carbon monoxide tolerance, which are both critical for alkaline direct ethanol fuel cell practical applications. This study paves the way for a novel approach for engineering high-performance, low-cost electrocatalysts that may be utilized as an alternative to commercial electrocatalysts in fuel cell technology.

Keywords Ethanol electrocatalytic oxidation · Platinum · Ruthenium · Polyaniline · Manganese ferrite

✉ Fatemeh Karimi
fkm024@gmail.com

✉ Mohammad Soleimani Lashkenari
m.soleimani@ausmt.ac.ir

✉ Ceren Karaman
cerenkaraman@akdeniz.edu.tr

Onur Karaman
onurkaraman@akdeniz.edu.tr

[1] Department of Chemical Engineering and Energy, Quchan University of Technology, 9477177870 Quchan, Iran

[2] Faculty of Chemical Engineering, Babol Noshirvani University of Technology, Shariati Ave., 47148-71167 Babol, Iran

[3] Fuel Cell Electrochemistry and Advanced Material Research Laboratory, Faculty of Engineering Modern Technologies, Amol University of Special Modern Technologies, 4616849767 Amol, Iran

[4] Chemical Engineering Department, Mazandaran University of Science and Technology, Babol, Mazandaran, Iran

[5] Department of Medical Imaging Techniques, Vocational School of Health Services, Akdeniz University, Antalya, Turkey

[6] Department of Electricity and Energy, Vocational School of Technical Sciences, Akdeniz University, Antalya, Turkey

Published online: 18 November 2021

1 Introduction

Fuel cells have drawn considerable attention as advanced energy-conversion systems in recent years, as the problem of fossil fuel scarcity and environmental pollution has become extremely serious. This is due to their high energy-utilization effectiveness and low pollutant emission properties [1–3]. Among various types of fuel cells, direct alcohol fuel cells (DAFCs) are considered to be a promising versatile and assistant control innovation, owing to the basic cell structure, lower running temperature, renewable capability, and high specific energy with low emissions [4]. Furthermore, the fluid ethanol as biofuel is very promising, due to its relatively higher biomass availablity, less toxic oxidation products compared to those from other alcohols, besides the high theoretical energy density value [5, 6].

Although direct ethanol fuel cells (DEFCs) have gained much more attention than other types of fuel cells, DEFC commercialization has been hampered by the poor performance of ethanol oxidation with currently available electrocatalysts. In this regard, high-performance ethanol oxidation catalysts are one of the most critical requirements for moving forward with energy conversion and storage applications [7].

Nanotechnology, which is generally defined as designed structures, devices and systems, has led to groundbreaking developments in many application areas thanks to the superior properties of the developed nanomaterials [8–17]. Nanomaterials with high-performance catalytic activity are very good choices in energy systems [8, 18–22]. Pt-based catalysts are thought to be the most promising competitors for the ethanol oxidation reaction in DEFCs, but their high price, insufficient precious metal resources, and poor stability caused by CO poisoning make them unsuitable for commercial applications [23]. Hence, recently, in an effort to overcome the mentioned problems, a wide range of extremely active Pt-based hybrid electrocatalysts containing a co-metal (like Ni, Bi, Ru, Sn and Pd) have been investigated by a few researches and utilized for the EOR in energy-conversion systems like high-performance DEFCs. Previous studies have shown that the Pt-based hybrid catalysts are capable of accelerating the ethanol oxidation reaction, reducing Pt loading, and increasing the Pt's CO tolerance. When compared to monometallic Pt, it is reported that Pt–Ru has displayed superior catalytic behavior and stability against EOR among the studied Pt alloys catalysts [1]. Because of its bi-functional mechanism and ligand effect (electronic effect), Ru is frequently utilized as a secondary metal to Pt in electrocatalysts (electronic effect). As the electronic structure of Pt is changed, the bond strength of poisoning intermediates on the Pt surface weakens, resulting in the ligand effect.

Recently, the spinel magnetic ferrites (MFe_2O_4:M = Ni^{2+}, Co^{2+}, Fe^{2+}, Mn^{2+}, Cu^{2+}, etc.) have been emerged widespread in a range of applications such as fuel cells. Among the spinel magnetic ferrites, $MnFe_2O_4$ has drawn substantial attention and been regarded as one of the most promising electrocatalysts thanks to their considerable advancement toward electrochemical reaction, cost-effectiveness, and environmental friendliness. Recently, Khan et al. [24] have employed Magnesium Ferrite ($MgFe_2O_4$) spinel structures prepared by a solid-state reaction as an anode modifier in the microbial fuel cell treatment of Congo red dye. In that study, the presence of the spinel structure in the electrode structure have helped to significant remediation of Congo red dye by improving the electrocatalytic activity of the electrode. In another effort, Tahir et al. [25] have utilized carbon felt electrode modified by $NiFe_2O_4$-MXene for enhancing the power generation of microbial fuel cells. The improvement reported in that study was somehow due to introducing an electrocatalysts structure like $NiFe_2O_4$. Despite the aforementioned advantages, the low conductivity and efficient surface area of $MnFe_2O_4$ limit its practical application for ethanol oxidation reaction, which consequences in the lower useful operating efficiency of DEFCs.

One can find several publications on boosting the capability of ethanol oxidation reaction by intergrading the catalysts with some conductive carriers such as MWCNT-COOH [26], N-doped carbon [27–29], and titanium dioxide nanosheets [30] and etc. Recently, Boulaghi et al. [2] presented a PPy/NGO hetero-structured as a catalysts support to improve the performance of Pt–Pd alloy as an appropriate anode catalyst for EOR in a DEFC. In another study, Kumar et al. [31] investigated Palladium nanoparticles decorated reduced graphene oxide (Pd-rGO) electrocatalysts for ethanol oxidation reaction and noticed that hybrid materials showed considerable behavior as electro-catalysts for EOR in DEFCs. Hence, selecting the right support material will facilitate the nanoparticle catalyst disperse well, prevent them from accumulating, reduce the amount of loading catalyst, besides expediting the electrochemical behavior, stability, and long-term operation [32]. In this respect, conductive polymers (CPs) have become intriguing in a variety of studies thanks to their peculiar physicochemical and electrochemical characteristics, which differentiate them from conventional semiconductors and metals [33]. Polyaniline (PANI) is among the most investigated conductive polymers, due to its advantageous properties such as ease of synthesis, cost-effectiveness, and strong adhesion to metal particles on its surface [34]. Decorating of PANI with $MnFe_2O_4$/Pt–Ru could exhibit the enhanced performance with obvious synergistic effects.

Bearing all in mind, in this work, it is aimed to resolve the aforementioned issues with DMFCs to improve operational performance. To the best of the authors' knowledge,

it is the first time that PANI-$MnFe_2O_4$/Pt–Ru nanocomposite was synthesized and investigated its potential utilization in alkaline direct ethanol fuel cells as an electrocatalyst. It was primarily aimed to get benefit from the synergistic effect of each component that composed the hybrid nanocomposite to boost the electrocatalytic performance of the commercial bimetallic electrocatalyst. To fabricate a hybrid structural PANI-$MnFe_2O_4$/Pt–Ru nanocomposite, a two-step production pathway has been suggested, in which Pt–Ru nanoparticles are uniformly dispersed on PANI-$MnFe_2O_4$ matrix and a clear heterojunction structure is obtained. The hybrid structure has been engineered to act as an effective electro-oxidation catalyst. The catalytic efficiency of PANI-$MnFe_2O_4$/Pt–Ru catalysts has been assessed using a number of electrochemical techniques including cyclic voltammetry (CV), linear sweep voltammetry (LSV), and Tafel, as well as chronoamperomerty (CA) techniques.

2 Experiment

2.1 Materials

Aniline ($C_6H_5NH_2$) (99%, d = 1.02 g/mL), potassium iodate (KIO_3), dihydrogen hexachloroplatinate (IV) hexahydrate ($H_2PtCl_6{\cdot}6H_2O$ 37.7%), ruthenium (III) chloride ($RuCl_3$) were purchased from Sigma–Aldrich. The aniline monomer was purified using a simple distillation process prior to the experiments. Polyvinylpyrrolidone and sulfuric acid (H_2SO_4, 98%), ethanol (CH_3–CH_2OH, 99.8%), potassium hydroxide (KOH), Iron(III) nitrate ($Fe(NO_3)_3{\cdot}9H_2O$, 99%), Manganese (II) nitrate ($Mn(NO_3)_2{\cdot}4H_2O$, 98.5%), sodium hydroxide (NaOH, 97%), were supplied from Merck.

2.2 Apparatus

The morphology investigations of nanocomposites were carried out through a scanning electron microscope (SEM, MIRA3TESCAN model XMU, Germany). Fourier transform infrared (FTIR) spectrometer (Shimadzu 4100, Japan) was employed for recording the FTIR spectra of the samples, at wavenumber ranging between 400 and 4000 cm^{-1}. The XRD analyses were collected by an X-ray powder diffractometer (X'Pert MPD, Netherlands) equipped with a Cu Kα radiation source (λ = 0.1542 nm).

The electro-oxidation experiments were conducted via a potentiostat/galvanostat instrument (PSGSTAT-204 Autolab (Metrohm, Netherlands)) at room temperature using a typical three-electrode electrochemical cell. An Ag/AgCl (in saturated KCl, reference electrode), a Pt wire (counter electrode), and a prepared electrode (working electrode) in which the hybrid catalyst was deposited on the electrode surface, were served in this ethanol electro-oxidation system. CV voltammograms were recorded in a solution of 1 M KOH and 1 M ethanol at a potential scan rate of 100 mVs^{-1}. LSV measurements were carried out in a 1 M KOH and 1 M ethanol solution in the potential range of 0.1 to − 0.9 V at a sweep rate of 50 mVs^{-1} to investigate the electrochemical behavior of ethanol oxidation on different electrodes. To analyze the EOR kinetics, Tafel plots were obtained using the linear sweep voltammetry technique. Moreover, the chronoamperometric (CA) responses were obtained to assess the stability of each catalyst in the solution of 1 M KOH and different concentrations of ethanol ranging from 0.1 to 2 M, as well as the current variation was evaluated.

2.3 Preparation of $MnFe_2O_4$ Nanoparticles

To make a homogeneously dispersed transparent metal–ion solution, 2.82 g $Fe(NO_3)_3{\cdot}9H_2O$ and 0.89 g $Mn(NO_3)_2{\cdot}4H_2O$ were dissolved in 50 ml deionized water. A magnetic stirrer was used to agitate the metal–ion dispersion until all of the reactants were thoroughly homogenously dissolved. The pH of the obtained suspension was then adjusted to 13 by adding 1 M of NaOH solution gradually. The temperature was maintained at 70 °C throughout stirring, and the reaction continued for 1 h. Finally, the solution was transferred to an autoclave, sealed, and kept at 180 °C for 16 h before being allowed to cool to ambient temperature. The product was centrifuged and rinsed in deionized water and 100% ethanol numerous times. Finally, the sample was dried in a 60 °C oven for 24 h [35].

2.4 Preparation of PANI Nanoparticles

In situ emulsion polymerization was conducted to prepare the PANI nanoparticles. To begin, 0.2 g polyvinylpyrrolidone (PVP) as a surfactant was dissolved in 100 mL sulfuric acid (1 M) solution under continuous stirring for *ca.*30 min in an ice bath at around 0 °C. Following that, 1.0 g KIO_3 as an initiator and 0.25 g $MnFe_2O_4$ nanoparticles were added to the previously prepared solution, which was then agitated for 30 min until all of the ingredients were fully disseminated. Finally, in an ice bath (0 °C), 1.0 mL of freshly distilled aniline monomer was gently added to the solution, and the mixture was agitated at 800 rpm for 20 h.

2.5 Preparation of PANI-$MnFe_2O_4$

The $MnFe_2O_4$ and PANI nanoparticles were fabricated using the techniques outlined in our previous study [35]. Subsequently, the PANI-$MnFe_2O_4$ nanocomposite was synthesized through in situ emulsion polymerization. Firstly, in an ice bath with a temperature of ca.0 °C, 0.2 g PVP as was dissolved in 100 mL sulfuric acid (1 M) solution under continuous stirring for almost 30 min. Subsequently, 1.0 g KIO_3 as

initiator and 0.25 g $MnFe_2O_4$ nanoparticles were introduced to as-prepared solution, which was then mixed for 30 min until the materials were fully dispersed. Finally, 1.0 mL of freshly distilled aniline monomer was slowly added to the solution in an ice bath (0 °C), and the mixture stirred at 800 rpm for 20 h. Afterward, the PANI-$MnFe_2O_4$ nanocomposite was separated by centrifuging of the resulting solution for 15 min at 6000 rpm, repeatedly, followed by the PANI-$MnFe_2O_4$ nanocomposite was washed with distilled water to remove the excess acid, and vacuum dried for 24 h at 60 °C.

2.6 Electrode Preparation

The graphite powder and an oil paraffin mixture were mixed in a 75:25 (w/w) weight ratio to prepare carbon paste electrode (CPE). Afterward, the CPE/PANI-$MnFe_2O_4$ electrode was prepared by hand blending the PANI-$MnFe_2O_4$ substrate (10% w/w) and the as-prepared CPE using a mortar and pestle until a homogenous paste was achieved. A glass tube with a length of 120 mm (∅ =4.65 mm) and a copper wire were utilized as a CPE preservative and electrical attachment, respectively. A CA approach was used to prepare the PANI-$MnFe_2O_4$/Pt–Ru-modified electrode. First, at a constant potential of − 0.5 V, Ru nanoparticles were electrodeposited for 100 s on the PANI-$MnFe_2O_4$ modifiedelectrode surface from a solution containing 0.05 M $RuCl_3$ and 0.5 M H_2SO_4. The electrochemical deposition of Pt nanoparticles on the PANI-$MnFe_2O_4$/Ru changed electrode was then carried out using a CA method in a solution comprising 0.035 M $H_2PtCl_6{\cdot}6H_2O$ and 0.5 M H_2SO_4 over 200 s at a constant potential of − 0.35 V. Finally, the as-prepared PANI-$MnFe_2O_4$/Pt–Ru was washed with distilled water before electrochemical tests.

3 Results and Discussion

3.1 Material Characterization

Figure 1 illustrates the surface morphologies of PANI-$MnFe_2O_4$ and PANI-$MnFe_2O_4$/Pt–Ru nanocomposites. As can be seen in Fig. 1a, the SEM image of PANI-$MnFe_2O_4$ shows flakes/sheets-like nanostructures of $MnFe_2O_4$ and PANI with a thin layer dispersed on the surface of $MnFe_2O_4$. PANI gross at the surface of $MnFe_2O_4$ as rod shape. This might be because the nanoparticles of $MnFe_2O_4$ serve as nuclei during the polymerization of aniline, resulting in the production of a PANI cluster. Figure 1b demonstrates the surface of the PANI-$MnFe_2O_4$/Pt–Ru electrode. As would be expected by implementing CV electro-deposition technique, a compact and smooth structure of Pt–Ru has been successfully deposited on the PANI-$MnFe_2O_4$ surface.

The FTIR spectra of PANI, $MnFe_2O_4$ and PANI-$MnFe_2O_4$ nanocomposite are represented in Fig. 2. The FTIR spectrum of PANI (Fig. 2a) displays bands at *ca.*1575 cm^{-1} and 1492 cm^{-1} refer to C=C stretching deformation of quinonoid and benzenoid units of PANI, respectively. The bands attributing to the C–N stretching of secondary amine in PANI chain, the in-plane bending vibration of C–H mode and the out-of-plane deformation of C–H in the benzene ring of PANI have emerged at *ca.*1294 cm^{-1}, 1137 cm^{-1}, and 797 cm^{-1}, respectively [36, 37]. Two main broad peaks corresponding to the intrinsic metal–oxygen stretching vibrations of octahedral and the tetrahedral sites are detected at around 413 cm^{-1} and 581 cm^{-1} in the FTIR spectrum of $MnFe_2O_4$ (Fig. 2b) [38]. Moreover, it is known that these absorption bands are typical of spinel ferrites in single phase. These findings are in line with the findings of earlier studies. On the other hand, the FTIR spectrum

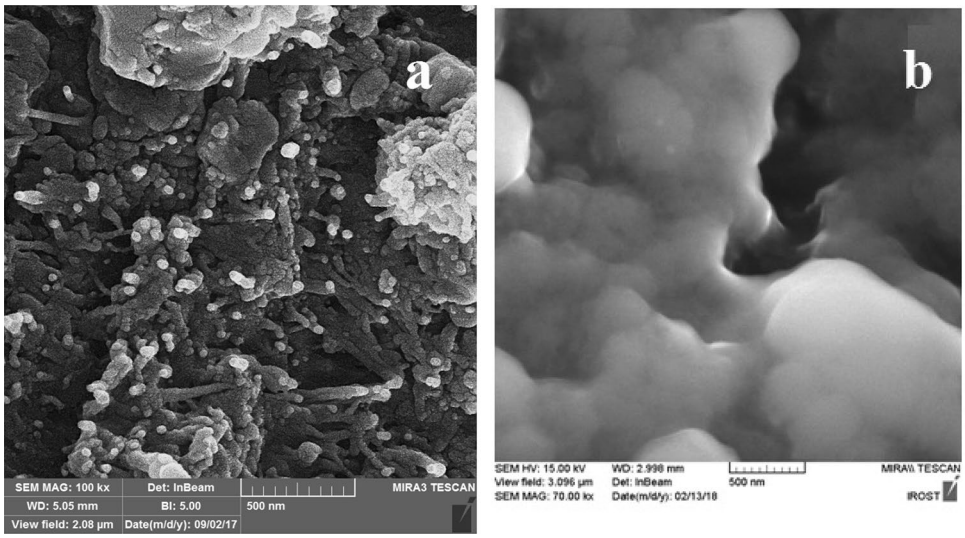


Fig. 1 SEM images of the **a** PANI-$MnFe_2O_4$, **b** PANI-$MnFe_2O_4$/Pt–Ru nanocomposites

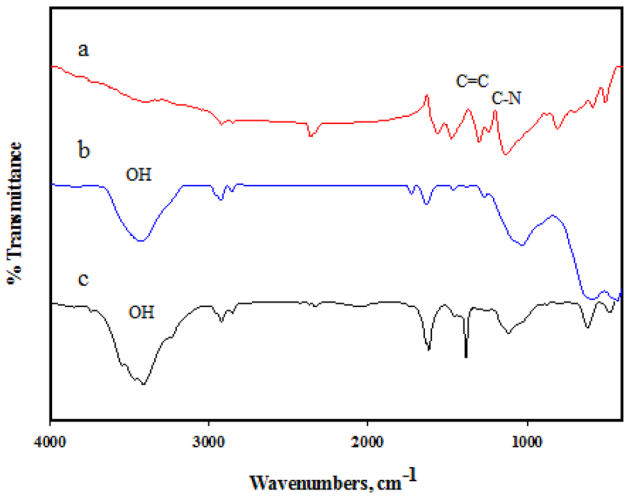


Fig. 2 FTIR spectra of (a) PANI (b) $MnFe_2O_4$ and (c) PANI-$MnFe_2O_4$ nanocomposite

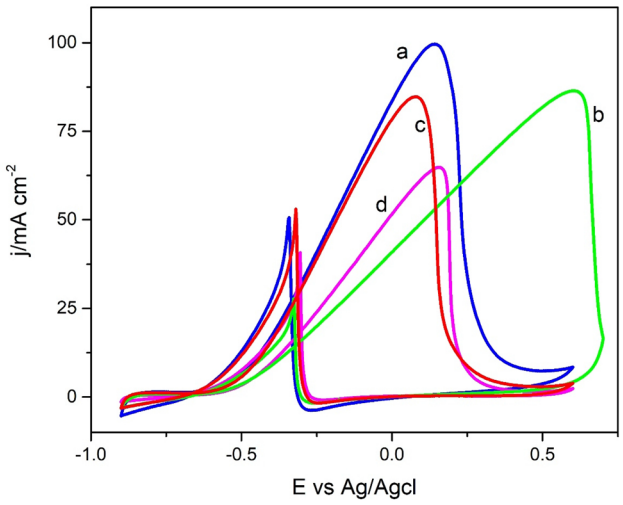


Fig. 4 CV voltammograms of (a) PANI-$MnFe_2O_4$/Pt–Ru, (b) PANI-$MnFe_2O_4$/Pt (c) Pt–Ru, and (d) Pt in 1 M KOH + 1 M C_2H_5OH

of the nanocomposite (Fig. 2c) exhibits the bands of both PANI (1575 cm^{-1}, 1492 cm^{-1}, 1294 cm^{-1}, 1137 cm^{-1} and 797 cm^{-1}) and $MnFe_2O_4$ (413 cm^{-1} and 583 cm^{-1}) with a minor shift indicating the interfacial interaction between the nitrogen atoms of PANI chains and the oxygen atoms of $MnFe_2O_4$ particles [39].

The crystallinity of the nanocomposites and nanoparticles has been investigated via XRD analysis. Figure 3a–d illustrates the XRD patterns of the PANI, $MnFe_2O_4$, PANI-$MnFe_2O_4$, and PANI-$MnFe_2O_4$/Pt–Ru. The broad peak with a maximum at ca. 2θ = 25° implies the amporphous structure

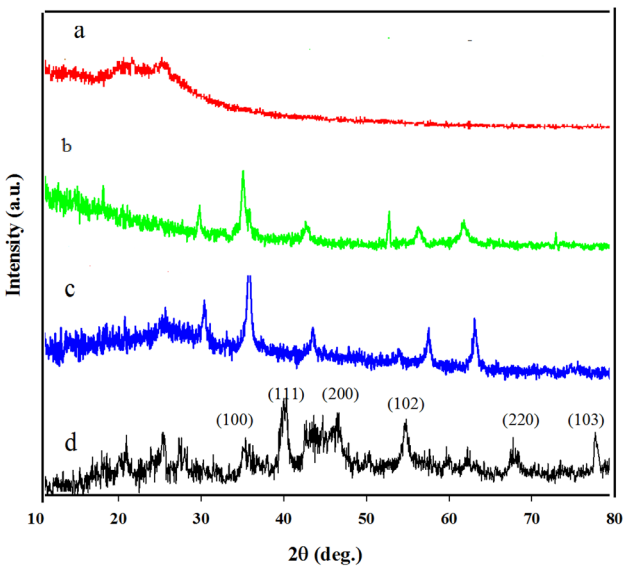


Fig. 3 XRD of (a) PANI (b) $MnFe_2O_4$ (c) PANI-$MnFe_2O_4$ and (d) PANI-$MnFe_2O_4$/Pt–Ru nanocomposite

of the PANI (Fig. 3a). In the case of $MnFe_2O_4$ pattern, the characteristic peaks have been observed at 2θ = 30.195°, 35.543°, 43.217°, 53.60°, 57.067°, 62.665° and 71.15° which are attributed to the (220), (311), (400), (422), (511), (440) and (533) reflection planes respectively. The cubic spinel nature of $MnFe_2O_4$ is determined by the identical diffraction peaks (Fig. 3b) agreeing well with the standard XRD data of $MnFe_2O_4$ (JCPDS card No. 10-0319). XRD patterns of PANI-$MnFe_2O_4$ nanocomposites (Fig. 3c) have revealed similar peaks to either $MnFe_2O_4$ and PANI which confirm cubic spinel structure of $MnFe_2O_4$ is retained during in-situ polymerization of PANI and successfully synthesis of the nanocomposite. The diffraction peaks of PANI-$MnFe_2O_4$/Pt–Ru (Fig. 3d) at 2θ of, 67.45, 46.48, and 40.06 are indexed as the (220), (200), and (111) planes of the FCC structure of crystalline Pt, respectively (PDF card No. 04-0802). Referring to Fig. 3d, the diffraction peaks at 2θ = 35.30º, 54.73º and 77.74º are aligned with the plane surfaces (100), (102) and (103) are related to Ru (JCPDS No. 65-7646). It can be concluded that the Pt and Ru nanoparticles have been successfully placed on the surface of the PANI-$MnFe_2O_4$ nanocomposite, depending on these findings and the alignment levels matching each other. There was no other XRD peak detected for other components. Thereby, the purity of the samples was also confirmed by the XRD analysis.

3.2 Electrochemical Measurements

3.2.1 CV Studies

EOR performance of PANI-$MnFe_2O_4$/Pt–Ru, PANI-$MnFe_2O_4$/Pt, Pt–Ru, and Pt electrocatalysts has been investigated in the solution of 1 M KOH and 1 M C_2H_5OH at

a potential scan rate of 100 mVs^{-1}. Figure 4 reveals that the oxidation of ethanol begins from the low onset potential ($E_{onset} = -0.65$ V), and reaches a wide oxidation peak at 0.1 V (vs. Ag/AgCl), after which the current declines owing to the formation of oxidized species that blocks the active sites. The CV voltammograms have indicated that the forward and reverse EOR polarization curves have two distinct current peaks. There are two well defined current peaks in the forward and reverse on EOR polarization curves. While the forward current (I_f) is principally responsible for the oxidation of chemisorbed ethanol species, carbonaceous species, which are not entirely oxidized during the forward scan, are removed oxidatively by the reverse scan currents [40]. It is clear that the I_f of the PANI-$MnFe_2O_4$/Pt–Ru (100 $mAcm^{-2}$) is higher than that of the Pt (64 $mAcm^{-2}$), Pt–Ru (85 $mAcm^{-2}$), and PANI-$MnFe_2O_4$/Pt (87 $mAcm^{-2}$).

The relatively negative shift of the E_{onset} and the remarkably high I_f are both indicators of excellent catalytic performance. The E_{onset} shifts from − 0.5 V (Pt) to − 0.65 V (PANI-$MnFe_2O_4$/Pt–Ru). (PANI-$MnFe_2O_4$/Pt–Ru) with the introduction of PANI-$MnFe_2O_4$. The synergistic effect of Ru also has an impact on the E_{onset}, which shifts from − 0.55 V at PANI-$MnFe_2O_4$/Pt to − 0.65 V at PANI-$MnFe_2O_4$/Pt–Ru. The remarkable negative shifting of E_{onset} suggests that the kinetics of the EOR have significantly boosted following the inclusion of PANI-$MnFe_2O_4$ and Ru. The PANI-$MnFe_2O_4$/Pt–Ru electrode has the highest current density and the lowest E_{onset}, indicating PANI-$MnFe_2O_4$/Pt–Ru electrode's outstanding catalytic activity when compared to the other electrodes. This phenomenon can be explained by the exceptionally conductive and porous nanostructure of the support material, which facilitate the charge transfer and ethanol molecules diffusion.

3.2.2 Electrochemically Active Surface Area (ECSA)

The Eq. 1 is used to determine the electrochemically active surface area, which is an essential aspect in evaluating the activity of electrocatalysts [41].

$$ECSA = \frac{Q_H}{0.21 m_{Pt}} \quad (1)$$

where Q_H stands for the charge for hydrogen adsorption (mC), which may be calculated by integrating the area under the CV curve for the hydrogen adsorption, m_{Pt} stands for Pt-loading (mg) in the electrode, and 0.21 ($mCcm^{-2}$) is the charge required to oxidize a monolayer of H_2 on brilliant Pt. ICP-OES analysis is conducted to identify the Pt loadings on the electrodes. It isfound that PANI-$MnFe_2O_4$/Pt–Ru, PANI-$MnFe_2O_4$/Pt, Pt–Ru, and Pt electrocatalysts have ECSA values of 30.3, 27.1, 21.4, and 15.2, respectively, based on hydrogen adsorption charge calculations from Fig. 5. Evidently, the precence of Ru and PANI-$MnFe_2O_4$ haveincreased the electrochemical active surface area.

3.2.3 Tafel Plots and Linear Sweep Voltammetry (LSV) Analysis

LSV curves have been recorded in 1 M KOH and 1 M C_2H_5OH solutions at a scan rate of 50 mVs^{-1} for all the as-prepared electrocatalysts to evaluate the EOR reaction mechanism. The LSV curves depicted in Fig. 6I offers some typical findings from such a study. The ethanol oxidation activity of PANI-$MnFe_2O_4$/Pt–Ru is significantly boosted, as evidenced by the negative shift of the E_{onset} and the increase in oxidation current [42]. Figure 6Π represents the Tafel plots of various electrocatalysts in the kinetic region of − 0.6 to − 0.4 V. The Tafel slope of PANI-$MnFe_2O_4$/Pt–Ru (161 $mVdec^{-1}$) is distinctly less than that PANI-$MnFe_2O_4$/Pt (164 $mVdec^{-1}$) and Pt–Ru (224 $mVdec^{-1}$) but larger than Pt (148 $mVdec^{-1}$) as shown in Fig. 6Π. The identical reaction mechanism for the rate-determining phase of ethanol oxidation (breaking of the first C–H bond of ethanol molecules) has been suggested by the same Tafel slope range (148–164 $mVdec^{-1}$) [43].

3.2.4 Ethanol Concentration

The effect of C_2H_5OH concentration on the effectiveness of PANI-$MnFe_2O_4$/Pt–Ru electrode has been examined by CV analysis in 1 M KOH solution containing different C_2H_5OH concentrations ranging between 0.1 M and 2.0 M (Fig. 7). The peak potential clearly moves towards more positive values as the ethanol concentration increases, demonstrating

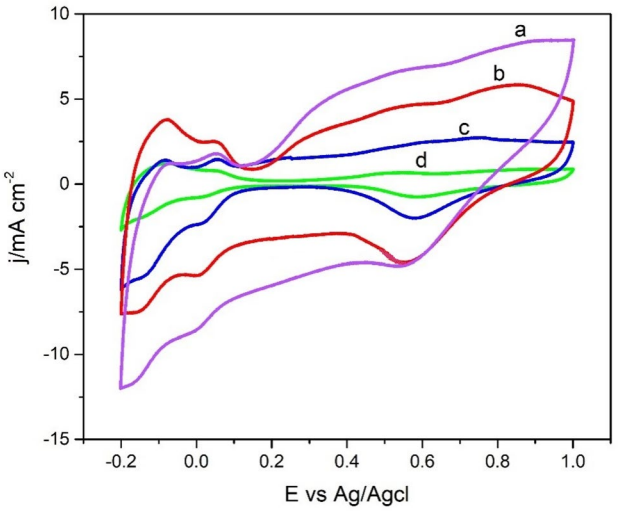


Fig. 5 CV voltammograms of (a) PANI-$MnFe_2O_4$/Pt–Ru, (b) PANI-$MnFe_2O_4$/Pt (c) Pt–Ru and (d) Pt in 1 M KOH solution at a potential scan rate of 50 mVs^{-1}

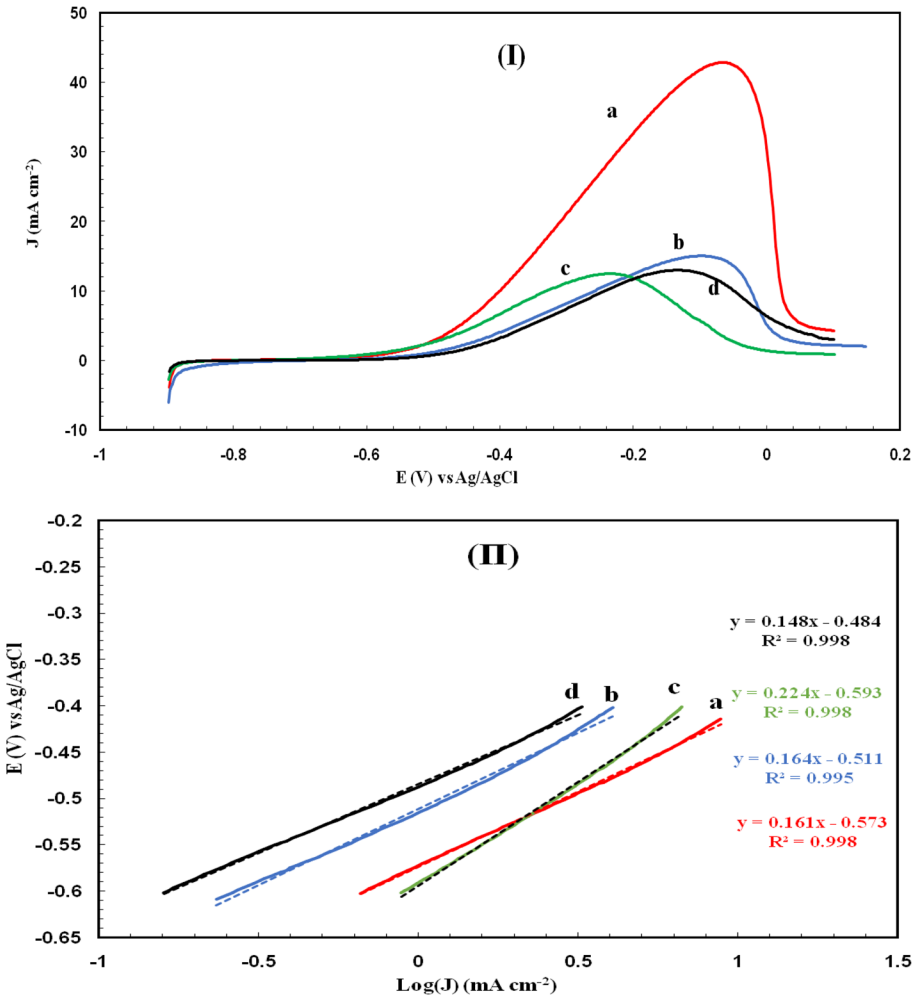


Fig. 6 LSV curves (I) and Tafel plots (II) of (a) PANI-$MnFe_2O_4$/Pt–Ru, (b) PANI-$MnFe_2O_4$/Pt (c) Pt–Ru and (d) Pt in a solution of 1 M KOH + 1 M C_2H_5OH at a potential scan rate of 50 mVs^{-1}

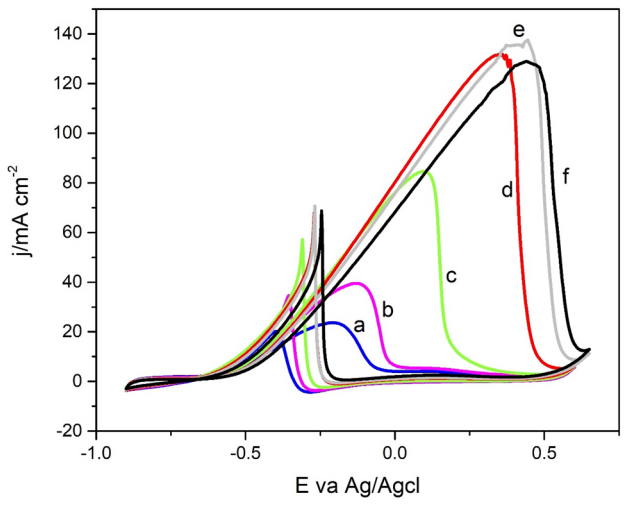


Fig. 7 CV voltammograms of PANI-$MnFe_2O_4$/Pt–Ru at (a) 0.1 M, (b) 0.2 M, (c) 0.5 M, (d) 1 M, (e) 1.5 M, and (f) 2 M ethanol concentrations in 1 M KOH solution

that EOR has been regulated by ethanol concentration at the electrode surface, and then drops at concentrations greater than 1.5 M. The saturation of active sites, the poisoning of the electrode surface with adsorbed intermediates such as CO_{ads}, and the existing of internal resistance (IR) drop due to increased oxidation current at higher concentrations might all explain these findings [44]. As a result of the excess availability of OH^{-1} ions, the peak currents are regulated by ethanol diffusion transport at low ethanol concentrations. Hence, the highest performance results have been obtained when the ethanol concentration is *ca.*1.5 M. In contrast, due to the abundant availability of ethanol and inadequate OH^{-1} ions at higher ethanol concentrations, the peak currents are controlled by diffusion transport of OH^{-1} ions.

3.2.5 Stability

The CA resoponses have been acquired in 1 M ethanol and 1 M KOH solution at a constant potential of 0.1 V to test long-term stability constant operation conditions, as shown in Fig. 8. The PANI-$MnFe_2O_4$/Pt–Ru, PANI-$MnFe_2O_4$/Pt

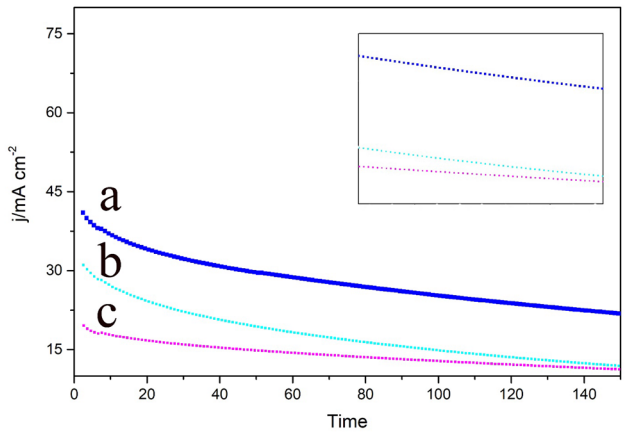


Fig. 8 Chronoamperograms of (a) PANI-$MnFe_2O_4$/Pt–Ru, (b) PANI-$MnFe_2O_4$/Pt, and (c) Pt in a solution of 1 M KOH + 1 M C_2H_5OH at a potential scan rate of 50 mVs^{-1} and constant potential of 0.1 V vs. Ag/AgCl

and Pt electrocatalysts have been tested for 300 s to assess their activity, stability and tolerance to poisoning by intermediate species. The formation of poisoning intermediate species such as CO_{ads} during EOR in an alkaline medium causes an initial current loss for all investigated catalysts [45]. The reaction on PANI-$MnFe_2O_4$/Pt–Ru has a lower current decay than other electrocatalysts, indicating that Pt–Ru on PANI-$MnFe_2O_4$ support material has improved long-term stability and tolerance to carbonaceous species formed during EOR.

A further benefit of cyclic voltammetry approaches is the ability to investigate the electrode stability across a wide range of potentials for several consecutive scans. Consequently, the effect of utilizing PANI-$MnFe_2O_4$ substrate on stability is evaluated by examining EOR of PANI-$MnFe_2O_4$/Pt–Ru and Pt–Ru electrode, through 100 consecutive CV scans in a solution of 1 M KOH and 1 M ethanol over a potential range of − 0.9 V to 0.5 V. The peak current density of PANI-$MnFe_2O_4$/Pt–Ru and Pt–Ru increases dramatically in the initial cycles (Fig. 9). The highest peak current density of the Pt–Ru/PANI-$MnFe_2O_4$ electrode has emerged around the 19th cycle, whereas the highest peak current density of the Pt–Ru electrode has appeared around the 5th cycle. The peak current densities of the PANI-$MnFe_2O_4$/Pt–Ru electrode then declined more slightly with increasing cycle number than those of the Pt–Ru electrode. After 100 cycles, PANI-$MnFe_2O_4$/Pt–Ru electrode retained around 94% of I_f, higher than Pt–Ru catalyst (89%). These findings have demonstrated that the activity and stability of the PANI-$MnFe_2O_4$/Pt–Ru electrocatalyst towards the ethanol-oxidation reaction have been improved significantly [46].

4 Conclusion

The goal of this work is to investigate the electrochemical behavior of the PANI-$MnFe_2O_4$ supported Pt–Ru electrocatalyst towards ethanol-oxidation in alkaline media. For this purpose, a number of electrochemical characterization techniques such as CA and CV, have been implemented. In comparison to the other electrodes, the PANI-$MnFe_2O_4$/Pt–Ru is found to be exceptional for boosting I_f value and increasing the electrochemically active surface area which is essential for ethanol molecules during the oxidation process.

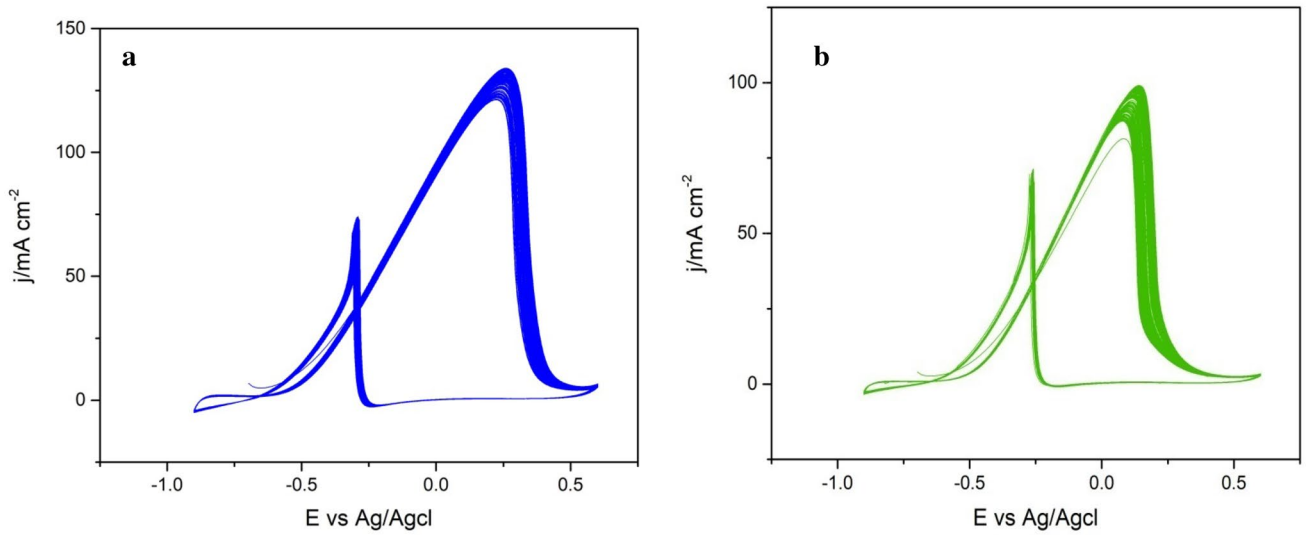


Fig. 9 CV voltammograms of **a** PANI-$MnFe_2O_4$/Pt–Ru, **b** Pt–Ru in 100 potential cycles in a solution of 1 M KOH + 1 M C_2H_5OH at a potential scan rate of 50 mVs^{-1}

The findings have proved that the synergistic effect of PANI-$MnFe_2O_4$ and Ru can facilitate the removing carbonaceous species adsorbed on Pt surfaces via ethanol electro-oxidation process. In terms of stability, 100 cycles and chronoamprommetry performance of the PANI-$MnFe_2O_4$/Pt–Ru indicates superior electrochemical stability and minimal capacitance loss, which might be owing to the superb resistance of the PANI-$MnFe_2O_4$/Pt–Ru to catalyst poisonous agents. This study not only discovered a potential electrocatalyst for EOR, but also a superior nanohybrid structure that can be applied to a variety of electrochemical applications and beyond. Furthermore, the current strategy provides a facile pathway for the synthesis of low-cost Pt-based nanomaterials, and it might have a wide range of applications in the technology of sustainable and renewable energy. In brief, it can be speculated that the work is noteworthy since the produced hybrid structure may be employed in fuel cells, such nanostructures are also prospective candidates for other applications such as sensors, photocatalysis, and energy storage devices.

References

1. Dong L, Gari RRS, Li Z, Craig MM, Hou S (2010) Graphene-supported platinum and platinum–ruthenium nanoparticles with high electrocatalytic activity for methanol and ethanol oxidation. Carbon 48(3):781–787
2. Boulaghi M, Taleghani HG, Lashkenari MS, Ghorbani M (2018) Platinum-palladium nanoparticles-loaded on N-doped graphene oxide/polypyrrole framework as a high performance electrode in ethanol oxidation reaction. Int J Hydrogen Energy 43(32):15164–15175
3. Karimi-Maleh H, Tahernejad-Javazmi F, Atar N, Yola MLT, Gupta VK, Ensafi AA (2015) A novel DNA biosensor based on a pencil graphite electrode modified with polypyrrole/functionalized multiwalled carbon nanotubes for determination of 6-mercaptopurine anticancer drug. Ind Eng Chem Res 54(14):3634–3639
4. Shafaei Douk A, Saravani H, Yazdan Abad MZ, Noroozifar M (2020) Three-dimensional engineering of nanoparticles to fabricate a Pd–Au aerogel as an advanced supportless electrocatalyst for low-temperature direct ethanol fuel cells. ACS Appl Energy Mater 3(8):7527–7534
5. Silva JCM, Ntais S, Rajaraman V, Teixeira-Neto É, Teixeira-Neto ÂA, Neto AO, Antoniassi RM, Spinacé EV, Baranova EA (2019) The catalytic activity of Pt: Ru nanoparticles for ethylene glycol and ethanol electrooxidation in a direct alcohol fuel cell. Electrocatalysis 10(3):203–213
6. Cunha E, Ribeiro J, Kokoh K, De Andrade A (2011) Preparation, characterization and application of Pt–Ru–Sn/C trimetallic electrocatalysts for ethanol oxidation in direct fuel cell. Int J Hydrogen Energy 36(17):11034–11042
7. Yang H, Geng L, Zhang Y, Chang G, Zhang Z, Liu X, Lei M, He Y (2019) Graphene-templated synthesis of palladium nanoplates as novel electrocatalyst for direct methanol fuel cell. Appl Surf Sci 466:385–392
8. Karaman C (2021) Boosting effect of nitrogen and phosphorous Co-doped three-dimensional graphene architecture: highly selective electrocatalysts for carbon dioxide electroreduction to formate. Top Catal. https://doi.org/10.1007/s11244-021-01500-6
9. Karaman C, Karaman O, Yola BB, Ulker İ, Atar N, Yola ML (2021) A novel electrochemical aflatoxin B1 immunosensor based on gold nanoparticles decorated porous graphene nanoribbon and Ag nanocubes incorporated MoS_2 nano. New J Chem 45(25):11222–11233. https://doi.org/10.1039/D1NJ02293H
10. Karaman O, Ozdogan H, Uncu VA, Karaman C, Tamar AG (2020) Investigation of the effects of different composite materials on neutron contamination caused by medical LINAC. Kerntechnik 85(5):401–407. https://doi.org/10.3139/124.200022
11. Karimi-Maleh H, Ayati A, Davoodi R, Tanhaei B, Karimi F, Malekmohammadi S, Orooji Y, Fu L, Sillanpaa M (2021) Recent advances in using of chitosan-based adsorbents for removal of pharmaceutical contaminants: a review. J Clean Prod. https://doi.org/10.1016/j.jclepro.2021.125880
12. Karimi-Maleh H, Karimi F, Fu L, Sanati AL, Alizadeh M, Karaman C, Orooji Y (2022) Cyanazine herbicide monitoring as a hazardous substance by a DNA nanostructure biosensor. J Hazard Mater 423:127058. https://doi.org/10.1016/j.jhazmat.2021.127058
13. Karimi-Maleh H, Orooji Y, Karimi F, Alizadeh M, Baghayeri M, Rouhi J, Tajik S, Beitollahi HD, Agarwal S, Gupta VK, Rajendran S, Ayati A, Fu L, Sanati AL, Tanhaei B, Sen F, Shabani-nooshabadi M, Asrami PN, Al-Othman A (2021) A critical review on the use of potentiometric based biosensors for biomarkers detection. Biosens Bioelectron 184:113252. https://doi.org/10.1016/j.bios.2021.113252
14. Karimi-Maleh H, Yola ML, Atar N, Orooji Y, Karimi F, Kumar PS, Rouhi J, Baghayeri M (2021) A novel detection method for organophosphorus insecticide fenamiphos: molecularly imprinted electrochemical sensor based on core-shell Co_3O_4@MOF-74 nanocomposite. J Colloid Interf Sci 592:174–185. https://doi.org/10.1016/j.jcis.2021.02.066
15. Korkmaz S, Kariper İA, Karaman O, Karaman C (2021) The production of rGO/RuO_2 aerogel supercapacitor and analysis of its electrochemical performances. Ceram Int. https://doi.org/10.1016/j.ceramint.2021.08.366
16. Al Sharabati M, Abokwiek R, Al-Othman A, Tawalbeh M, Karaman C, Orooji Y, Karimi F (2021) Biodegradable polymers and their nano-composites for the removal of endocrine-disrupting chemicals (EDCs) from wastewater: a review. Environ Res. https://doi.org/10.1016/j.envres.2021.111694
17. Boke CP, Karaman O, Medetalibeyoglu H, Karaman C, Atar N, Yola ML (2020) A new approach for electrochemical detection of organochlorine compound lindane: development of molecular imprinting polymer with polyoxometalate/carbon nitride nanotubes composite and validation. Microchem J. https://doi.org/10.1016/j.microc.2020.105012
18. Karaman C, Karaman O, Atar N, Yola ML (2021) Sustainable electrode material for high-energy supercapacitor: biomass-derived graphene-like porous carbon with three-dimensional hierarchically ordered ion highways. Phys Chem Chem Phys 23(22):12807–12821
19. Aykan A, Karaman O, Karaman C, Atar N, Yola ML (2021) A comparative study of CO catalytic oxidation on the single vacancy and di-vacancy graphene supported single-atom iridium catalysts: a DFT analysis. Surfaces Interfaces 25:101293
20. Karaman C, Bayram E, Karaman O, Aktaş Z (2020) Preparation of high surface area nitrogen doped graphene for the assessment of morphologic properties and nitrogen content impacts on supercapacitors. J Electroanal Chem 868:114197
21. Ensafi AA, Karimi-Maleh H, Mallakpour S (2011) N-(3,4-Dihydroxyphenethyl)-3,5-dinitrobenzamide-modified multiwall carbon nanotubes paste electrode as a novel sensor for simultaneous determination of penicillamine, uric acid, and tryptophan. Electroanalysis 23(6):1478–1487. https://doi.org/10.1002/elan.201000741

22. Karimi-Maleh H, Keyvanfard M, Alizad K, Fouladgar M, Beitollahi H, Mokhtari A, Gholami-Orimi F (2011) Voltammetric determination of N-actylcysteine using modified multiwall carbon nanotubes paste electrode. Int J Electrochem Sc 6(12):6141–6150
23. Pieta IS, Rathi A, Pieta P, Nowakowski R, Hołdynski M, Pisarek M, Kaminska A, Gawande MB, Zboril R (2019) Electrocatalytic methanol oxidation over Cu, Ni and bimetallic Cu-Ni nanoparticles supported on graphitic carbon nitride. Appl Catal B 244:272–283
24. Khan N, Anwer AH, Khan MD, Azam A, Ibhadon A, Khan MZ (2021) Magnesium ferrite spinels as anode modifier for the treatment of Congo red and energy recovery in a single chambered microbial fuel cell. J Hazard Mater 410:124561
25. Tahir K, Miran W, Jang J, Maile N, Shahzad A, Moztahida M, Ghani AA, Kim B, Jeon H, Lim S-R (2021) Nickel ferrite/MXene-coated carbon felt anodes for enhanced microbial fuel cell performance. Chemosphere 268:128784
26. Parreira LS, Antoniassi RM, Freitas IC, de Oliveira DC, Spinacé EV, Camargo PH, dos Santos MC (2019) MWCNT-COOH supported PtSnNi electrocatalysts for direct ethanol fuel cells: low Pt content, selectivity and chemical stability. Renew Energy 143:1397–1405
27. Miyawaki T, Tobiishi K, Takenaka S, Kadokami K (2018) A rapid method, combining microwave-assisted extraction and gas chromatography-mass spectrometry with a database, for determining organochlorine pesticides and polycyclic aromatic hydrocarbons in soils and sediments. Soil Sediment Contamination: An Int J 27(1):31–45
28. Zhang Z, Wu Q, Mao K, Chen Y, Du L, Bu Y, Zhuo O, Yang L, Wang X, Hu Z (2018) Efficient ternary synergism of platinum/tin oxide/nitrogen-doped carbon leading to high-performance ethanol oxidation. ACS Catal 8(9):8477–8483
29. Shi W, Wang Q, Qin F, Yu J, Jia M, Gao H, Zhang Y, Zhao Y, Li G (2017) N-doped carbon encapsulated nickel nanoparticles: rational fabrication and ultra-high performance for ethanol oxidation. Electrochim Acta 232:332–338
30. Wu T, Fan J, Li Q, Shi P, Xu Q, Min Y (2018) Palladium nanoparticles anchored on anatase titanium dioxide-black phosphorus hybrids with heterointerfaces: highly electroactive and durable catalysts for ethanol electrooxidation. Adv Energy Mater 8(1):1701799
31. Kumar R, da Silva ET, Singh RK, Savu R, Alaferdov AV, Fonseca LC, Carossi LC, Singh A, Khandka S, Kar KK (2018) Microwave-assisted synthesis of palladium nanoparticles intercalated nitrogen doped reduced graphene oxide and their electrocatalytic activity for direct-ethanol fuel cells. J Colloid Interface Sci 515:160–171
32. Mozafari V, Parsa JB (2020) Electrochemical synthesis of Pd supported on PANI-MWCNTs-SnO_2 nanocomposite as a novel catalyst towards ethanol oxidation in alkaline media. Synth Met 259:116214
33. Lashkenari MS, Ghorbani M, Silakhori N, Karimi-Maleh H (2021) Enhanced electrochemical performance and stability of Pt/Ni electrocatalyst supported on SiO_2-PANI nanocomposite: a combined experimental and theoretical study. Mater Chem Phys 262:124290
34. Nodehi Z, Rafati AA, Ghaffarinejad A (2018) Palladium-silver polyaniline composite as an efficient catalyst for ethanol oxidation. Appl Catal A 554:24–34
35. Kafshgari LA, Ghorbani M, Azizi A (2017) Fabrication and investigation of $MnFe_2O_4$/MWCNTs nanocomposite by hydrothermal technique and adsorption of cationic and anionic dyes. Appl Surf Sci 419:70–83
36. Wang P-C, Dan Y, Liu L-H (2014) Effect of thermal treatment on conductometric response of hydrogen gas sensors integrated with HCl-doped polyaniline nanofibers. Mater Chem Phys 144(1):155–161
37. Kotresh S, Ravikiran Y, Vijayakumari S, Thomas S (2017) Interfacial pn heterojunction of polyaniline-nickel ferrite nanocomposite as room temperature liquefied petroleum gas sensor. Compos Interfaces 24(6):549–561
38. Kooti M, Sedeh AN (2013) Synthesis and characterization of $NiFe_2O_4$ magnetic nanoparticles by combustion method. J Mater Sci Technol 29(1):34–38
39. Nasirian S, Moghaddam HM (2014) Effect of different titania phases on the hydrogen gas sensing features of polyaniline/TiO_2 nanocomposite. Polymer 55(7):1866–1874
40. Kabir S, Serov A, Artyushkova K, Atanassov P (2016) Design of novel graphene materials as a support for palladium nanoparticles: highly active catalysts towards ethanol electrooxidation. Electrochim Acta 203:144–153
41. Tan JL, De Jesus AM, Chua SL, Sanetuntikul J, Shanmugam S, Tongol BJV, Kim H (2017) Preparation and characterization of palladium-nickel on graphene oxide support as anode catalyst for alkaline direct ethanol fuel cell. Appl Catal A 531:29–35
42. Dutta A, Mondal A, Broekmann P, Datta J (2017) Optimal level of Au nanoparticles on Pd nanostructures providing remarkable electro-catalysis in direct ethanol fuel cell. J Power Sources 361:276–284
43. Hameed RA (2017) Enhanced ethanol electro-oxidation reaction on carbon supported Pd-metal oxide electrocatalysts. J Colloid Interface Sci 505:230–240
44. Rahim MA, Hameed RA, Khalil M (2004) Nickel as a catalyst for the electro-oxidation of methanol in alkaline medium. J Power Sources 134(2):160–169
45. Zhang K, Bin D, Yang B, Wang C, Ren F, Du Y (2015) Ru-assisted synthesis of Pd/Ru nanodendrites with high activity for ethanol electrooxidation. Nanoscale 7(29):12445–12451
46. Feng Y, Bin D, Yan B, Du Y, Majima T, Zhou W (2017) Porous bimetallic PdNi catalyst with high electrocatalytic activity for ethanol electrooxidation. J Colloid Interface Sci 493:190–197

Publisher's Note Springer Nature remains neutral with regard to jurisdictional claims in published maps and institutional affiliations.